# Chapter 7

# Multiple local symmetries triggering zero/negative thermal expansion in morphotropic relaxor boundary

## 7.1 Introduction

Crystal structure plays a crucial role in determining the dielectric properties of materials, including ferroelectricity, piezoelectricity, flexoelectricity, pyroelectricity, etc. [320, 321, 322, 323]. The atomic arrangement within a material significantly influences these properties and can be modified through compositional engineering. Strategically adjusting the compositions to achieve high physical properties over a broad temperature range is a defining feature of morphotropic phase boundaries (MPB) and disordered/relaxor ferroelectrics (RFE) [7, 57, 58]. MPB refers to a composition-driven phase boundary between two distinct long-range ordered ferroelectric phases coexisting for a wide temperature range [54, 57, 58, 212]. Likewise, RFEs are disordered dielectric materials known for their high dielectric constant across an extensive temperature spectrum. RFEs generally exhibit a centrosymmetric, non-polar cubic phase at long ranges with a non-centrosymmetric, polar phase at short ranges [5, 7, 116, 118, 137, 324]. A recently discovered structural phenomenon, known as morphotropic relaxor boundary (MRB), integrates the characteristics of MPB (two-phase coexistence along with weak temperature dependence) with RFE (distinct atomic ordering at long and short ranges stable for a wide temperature range) [15]. Subsequently, MRB is defined as a boundary between two polar/ferroelectric phases coexisting at short ranges within an average cubic phase at long ranges stable for a wide temperature range [15, 61, 182]. Notably, the dielectric constant and electrostrain are enhanced in the vicinity of recently discovered $K_{0.5}Na_{0.5}NbO_3$-based MRB, where tetragonal and rhombohedral phases co-exist at short ranges in an average cubic structure [15].

Disordered/relaxor ferroelectrics are known to exhibit electrostrictive and ferroelectrostrictive properties, which may result in negative or zero thermal expansion (NTE/ZTE) [7, 118, 284, 286, 287]. Increasing the polar/ferroelectric content of short-range ferroelectric regions in RFE materials can enhance thermal stability, particularly by achieving volume gain *via* ferroelectrostriction [7, 118]. NTE/ZTE plays a vital role in maintaining thermal stability for various modern electronic high precision instruments, multi-layer ceramic capacitors, thin film devices, etc [19, 299]. Therefore, investigating the influence of recently coined MRB on the thermal expansion of Pb-free disordered/relaxor materials could open new avenues for eco-friendly smart materials.

In the present work, we have discovered a unique morphotropic relaxor boundary (MRB) with two polar symmetries *viz.*, monoclinic and rhombohedral at short ranges coexisting for a wide temperature range in $Ba_{0.9}Sr_{0.1}TiO_3$ (BST10) doped KNN50 *viz.*, (1-$x$)KNN50-$x$BST10 (KBST$x$) for $0.20 \leq x \leq 0.90$. Here, we have chosen Pb-free parents *viz.*, KNN50 and BST10 due to the presence of MPB in KNN50 [8, 53, 212] and high dielectric constant of BST10 [64, 66]. The long-range ordering of KBST$x$ is determined using X-ray diffraction data, while the short-range ordering is explored using

Raman scattering and pair distribution function data. The high-energy synchrotron X-ray diffraction and pair distribution function data has been taken at 39 temperatures in the range of 8 K $\leq T \leq$ 495 K. Subsequently, NTE/ZTE is determined/quantified at long ranges using temperature-dependent synchrotron X-ray diffraction data, and its origin is uncovered by pair distribution function analysis.

## 7.2 Experimental procedure

The KBST$x$ ($0.20 \leq x \leq 0.90$) ceramics have been synthesized using a solid-state reaction method. The precursors *viz.*, $K_2CO_3$ (Sisco Research Laboratories Pvt. Ltd.) (99%), $Na_2CO_3$ (HIMIDEA Labs) (99.5%), $BaCO_3$ (HIMIDEA Labs) (99%), $SrCO_3$ (HIMIDEA Labs) (99%), $Nb_2O_5$ (HIMIDEA Labs) (99.9%), and $TiO_2$ (HIMIDEA Labs) (99%) were pre-heated in an oven at 393 K. The heated powders were weighed in a stoichiometric ratio and milled in a planetary ball mill (Retsch PM 200) for 24 hours for homogeneous mixing. After milling, the powder slurry was dried and calcined at temperatures in the range of 1123 K - 1173 K for 4-6 hours. The pellets were formed at 8-10 metric tons pressure and sintered at 1388 K - 1423 K for 3-4 hours. The long-range crystal structures were determined using X-ray diffraction data which was collected for a wide $2\theta$ range (20° to 120°) and step size of 0.02 by Rikagu Miniflex 600 X-ray diffractometer having Cu-$K_\alpha$ radiation. The temperature-dependent dielectric data of KBST$x$ ceramics has been obtained using an LCR meter by Keysight technologies. Further, to determine the short-range symmetries, temperature-dependent Raman scattering data was collected using a Horiba LabRAM HR Raman spectrometer with an Olympus BX41 microscope attachment having an excitation wavelength of 514.5 nm from an argon ion laser (Lexel Model-95). Moreover, high-energy ($\lambda \approx 0.1665$ Å) temperature-dependent Synchrotron X-ray diffraction (SXRD) data has been obtained from Brookhaven National Lab for KBST40 over a broad temperature range (8 K $\leq T \leq$ 495 K).

The pair distribution function (PDF) data was obtained from the high-energy SXRD data in the following way. Firstly, the intensity of the diffraction data was reduced to total scattering structure function S(Q) [208, 211]:

$$S(Q) = 1 + \frac{[I_{\mathrm{coh}}(Q) - \sum c_{\mathrm{i}}|f_{\mathrm{i}}(Q)|^2]}{|\sum f_{\mathrm{i}}(Q)c_{\mathrm{i}}|^2} \tag{7.1}$$

where Q = $4\pi\sin\theta/\lambda$, $2\theta$ is the angle between incident and diffracted beams, $I_{\mathrm{coh}}(Q)$ corresponds to the coherent part of the diffraction data while $c_{\mathrm{i}}$ and $f_{\mathrm{i}}(Q)$ are the atomic concentrations and x-ray structure factor of $i^{\mathrm{th}}$ atomic species.

Secondly, S(Q) was transformed into pair distribution function G(r) *via* Fourier transformation with $Q_{\mathrm{max}}$ = 27.8 Å$^{-1}$ [208, 211]:

$$G(r) = \frac{2}{\pi}\int_{Q_{\mathrm{min}}}^{Q_{\mathrm{max}}} Q[S(Q) - 1]sin(Qr)dQ \tag{7.2}$$

Further, the decomposition of phonon modes has been done using *ISODISTORT* software available online [258, 315].

## 7.3 Results and discussions

### 7.3.1 X-ray diffraction analysis of KBST*x* ceramics

The long-range crystal structures of KBST*x* ceramics for $0.20 \leq x \leq 0.90$ has been determined using X-ray diffraction data. Figure 7.1 depicts the evolution of the main perovskite peaks *viz.*, {200}, {220}, and {222} as a function of composition (*x*). All of the main perovskite peaks exhibit a singlet nature for $0.20 \leq x \leq 0.90$ (see Fig.7.1), suggesting an average cubic symmetry for KBST*x* ceramics. Moreover, an additional broadening in the tails of the main perovskite peaks is clearly evident in Fig. 7.1 (see black arrows in Fig. 7.1), suggesting disorder in the material, which is similar to what

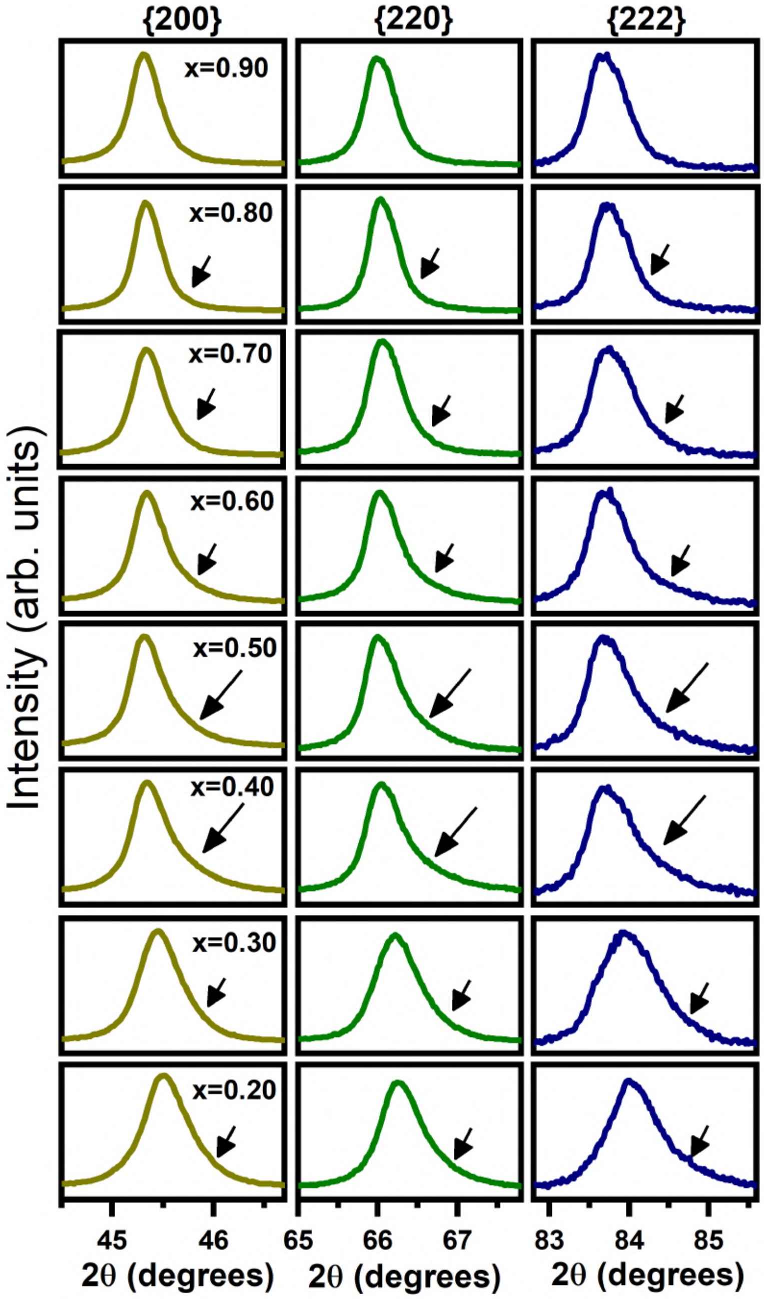

Fig. 7.1 The evolution of {200}, {220}, and {222} X-ray diffraction peak profiles for KBST$x$ ($0.20 \leq x \leq 0.90$) ceramics. The black arrows indicate the additional broadening in the tails of the main perovskite peaks. The length of the arrows suggests the relative magnitude of the disorder in KBST$x$ ceramics.

has been observed for other disordered perovskite materials like Pb(Mg, Nb)$O_3$ (PMN) [242, 260, 325], (K,Na,Ba,Sr)(Nb,Ti)$O_3$ [7], etc. This disorder is quantified using FWHM of the peak associated with additional broadening (obtained after deconvolution of the main perovskite peaks; see Fig. 7.2(a)) and compared as a function of composition ($x$) (see Fig. 7.2(b)). The maximum FWHM has been observed for $x = 0.40$ (KBST40), suggesting highest disorder for KBST40 ceramics (see Fig. 7.2(b)). The disorder present in the material has been attributed to the chemical heterogeneity (*i.e.*, elements having different ionic radii and oxidation states placed at A/B-sites respectively), thereby suggesting the presence of short-range order in an average cubic symmetry [325]. The short-range order is determined using Raman scattering and pair distribution function data in the subsequent sections.

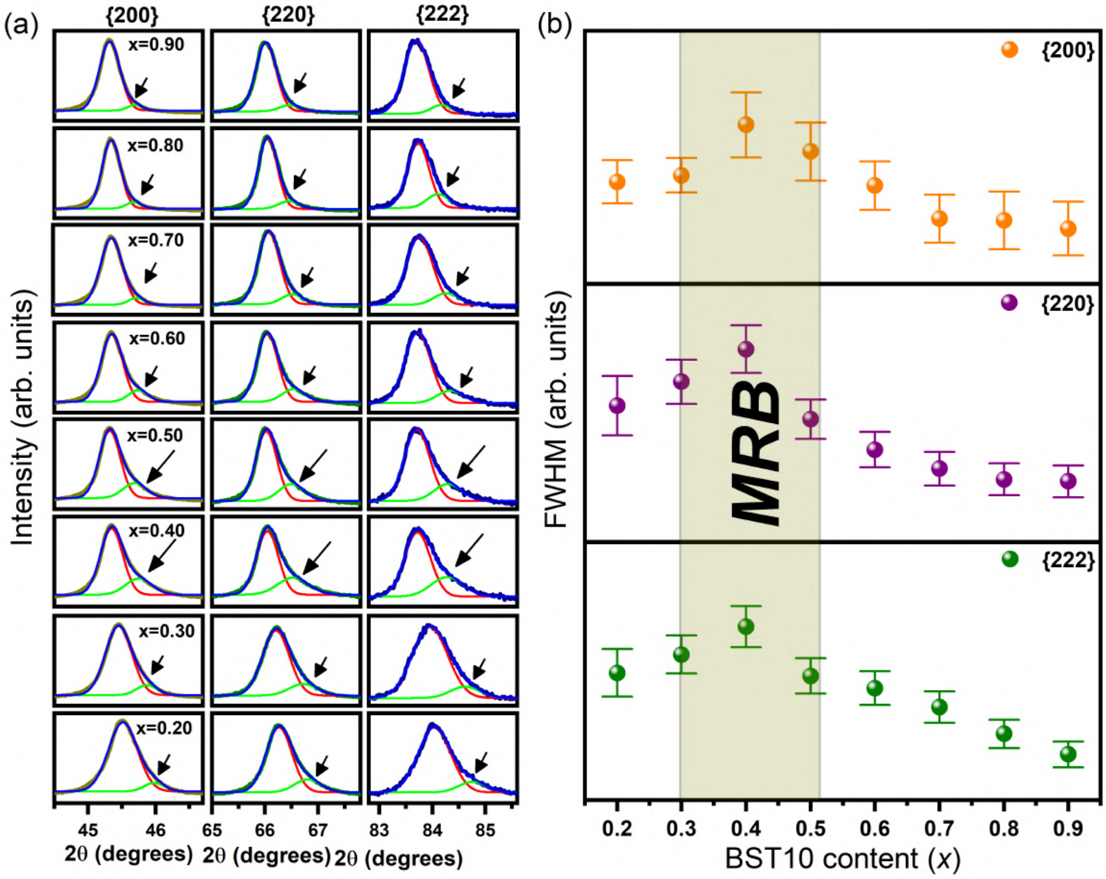

Fig. 7.2 (a) Deconvolution of main perovskite peaks *viz*., {200}, {220}, and {222}, and (b) Evolution of FWHM of the peak associated with additional broadening (green peak) as a function of composition ($x$) .

## 7.3.2 Raman spectroscopic studies

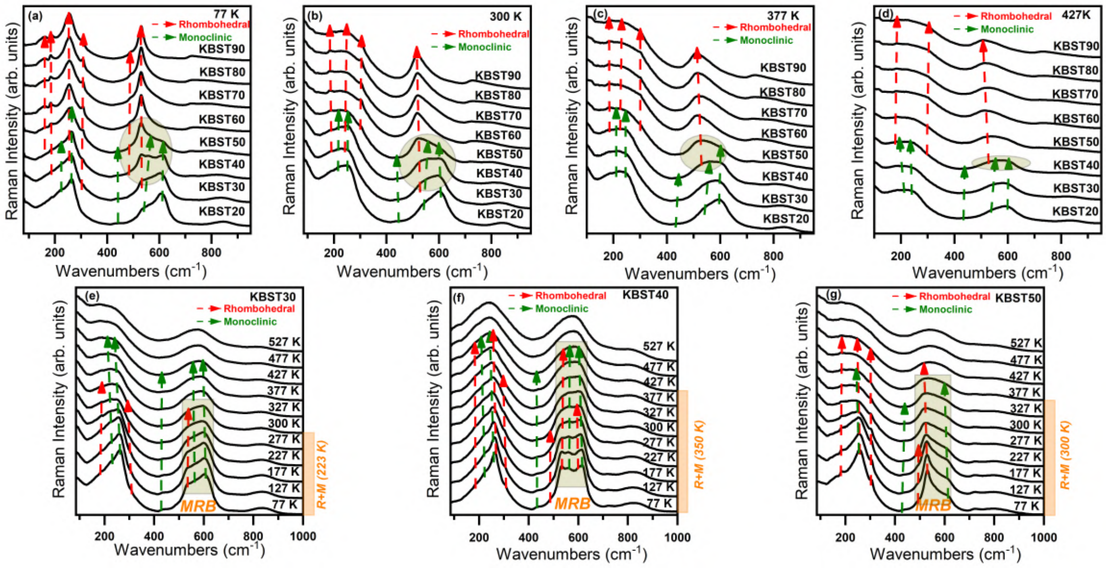

Fig. 7.3 The top figures represent the evolution of Raman scattering data as a function of compositions at representative temperatures *i.e.*, (a) 77 K, (b) 300 K, (c) 377 K, and (d) 427 K. The bottom figures represent the temperature-dependent Raman scattering data for (e) KBST30, (f) KBST40, and (g) KBST50 ceramics.

Raman scattering is a powerful technique and can probe internal vibrations of $BO_6$ octahedra, thereby revealing short-range ordering (if any), and complementing or corroborating the results obtained from conventional X-ray/neutron diffraction data [21, 202]. Figures 7.3(a)-(d) depicts the Raman spectra of KBST$x$ ceramics at some representative temperatures *viz.*, 77 K, 300 K, 377 K, and 427 K. The composition-dependent Raman spectra at 77 K depicts monoclinic symmetry for KBST20 [7] (KNN50 rich composition) and rhombohedral symmetry for KBST90 [118] ($BaTiO_3$ (BT) rich composition [206]) (see Fig.7.3(a)). In between the two extremes *viz.*, KBST20 and KBST90, a co-existence of two polar symmetries at short ranges *viz.*, monoclinic and rhombohedral has been observed for KBST30, KBST40, and KBST50 (see Fig.7.3(a)). The two-phase coexistence is also observed at room temperature for KBST30, KBST40, and KBST50 (see Fig.7.3(b)), suggesting the presence of a morphotropic relaxor boundary (MRB) [15]. Among the three compositions exhibiting two-phase co-existence at room temperature, the convoluted peak corresponding to stretching modes ($\nu_s \approx 500$ cm$^{-1}$ to $\approx 600$ cm$^{-1}$) demonstrates maximum width (or disorder) [202] for KBST40 (see Fig.7.3(b)), thereby corroborating the conclusions drawn from X-ray diffraction analysis. The two-phase coexistence as a function of composition ($x$) describes the horizontal width ($\Delta x$) (where $0.20 < x < 0.60$ at ambient conditions) of MRB at any particular temperature. Moreover, at 377 K, the horizontal width of MRB shrinks, and only two compositions *viz.*, KBST40 and KBST50 demonstrate two-phase co-existence (see Fig.7.3(c)). Subsequently, at 427 K, only KBST40 exhibits two-phase co-existence (see Fig.7.3(d)). Further, in order to determine two-phase co-existence as a function of temperatures (*i.e.*, vertical width; ΔT), we have plotted the Raman spectra of KBST30, KBST40, and KBST50 ceramics for 77 K $\leq T \leq$ 527 K (see Figs. 7.3(e)-(g)). Firstly, for KBST30, the two polar phases co-exist for 77 K $\leq T \leq$ 300 K ($\Delta T_{R+M}$ = 223 K) (see Fig. 7.3(e)). Here, $\Delta T_{R+M}$ is the vertical width corresponding to monoclinic (M) and rhombohedral (R) phases. Moreover, above 300 K, only monoclinic phase remains, which is stable up to 427 K (see Fig. 7.3(e)). Secondly, for KBST40, the two polar phases coexist for 77 K $\leq T \leq$ 427 K, resulting in an increase in vertical width *i.e.*, $\Delta T_{R+M}$ = 350 K (see Fig. 7.3(f)). Lastly, vertical width ($\Delta T_{R+M}$ = 300 K) decreases for KBST50, and the two polar phases co-exist for 77 K $\leq T \leq$ 377 K (see Fig. 7.3(g)). Therefore, the vertical width ($\Delta T_{R+M}$ = 350 K) is maximum for KBST40. Thus, the coexistence of two polar phases *viz.*, monoclinic and rhombohedral at short ranges (determined using Raman spectroscopy) in an average cubic symmetry at long ranges (determined using X-ray diffraction), confirms MRB for $0.20 < x < 0.60$ with a maximum vertical width ($\Delta T_{R+M}$ = 350 K) for KBST40. The vertical width observed for MRB compositions of KBST$x$ has been attributed to the stability of multiple local symmetries in an average cubic symmetry [7, 118, 326]. Moreover, Figure 7.4 depicts the temperature-dependent Raman spectra of KBST$x$ ceramics for $0.20 \leq x \leq 0.90$. The green and red arrows represent the peaks corresponding to monoclinic and rhombohedral symmetry, respectively. The highlighted temperature (in orange color) corresponds to the Burns temperature ($T_B$), below which nucleation and growth of polar nanoregions begin.

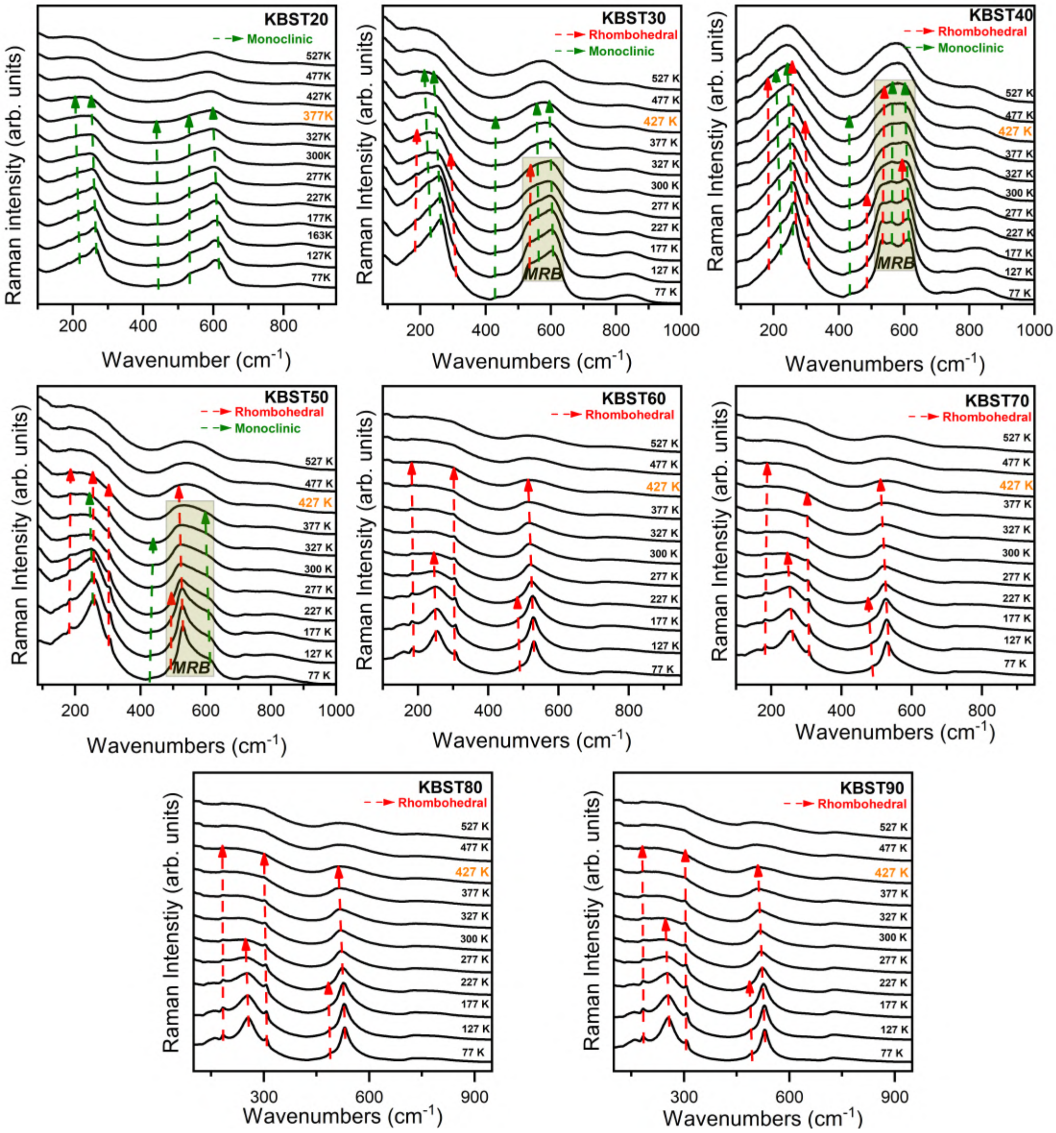

Fig. 7.4 Temperature-dependent evolution of Raman spectra of KBST$x$ ceramics for $0.20 \leq x \leq 0.90$. The highlighted temperature (in orange color) represents Burns temperature ($T_B$) for KBST$x$ ceramics.

Further, owing to the maximum vertical width ($\Delta T_{R+M}$ = 350 K) linked with maximum disorder (see Fig. 7.3(b) and Fig. 7.2) for KBST40, temperature-dependent pair distribution function (PDF) analysis was employed to ascertain the symmetry of the two phases and further ferroelectric content of the two polar phases was quantified using mode crystallography [118, 212, 227].

### 7.3.3 Pair distribution function analysis of KBST40 ceramics

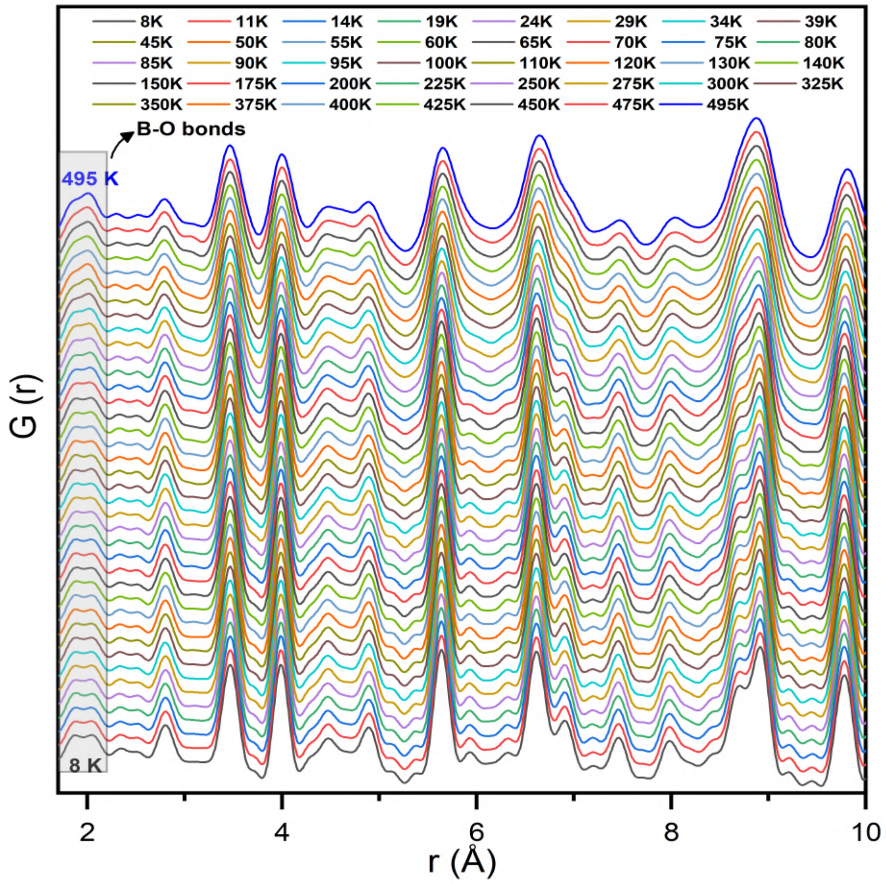

Fig. 7.5 Temperature-dependent observed G(r) patterns of KBST40 ceramics..

The temperature-dependent pair distribution function (PDF) data of KBST40 has been obtained for 8 K $\leq T \leq$ 495 K (see Fig. 7.5). Considering two different polar symmetries observed in the temperature-dependent Raman scattering data, we have used three plausible models *viz.*, (i) monoclinic (Space Group: $Pm$), (ii) rhombohedral (Space Group: $R3m$), and (iii) monoclinic + rhombohedral ($Pm + R3m$) to fit the PDF data collected at 8 K using PDFGUI software [213]. Figure 7.6(a) depicts PDF profile fitting of KBST40 at 8 K for 1.7

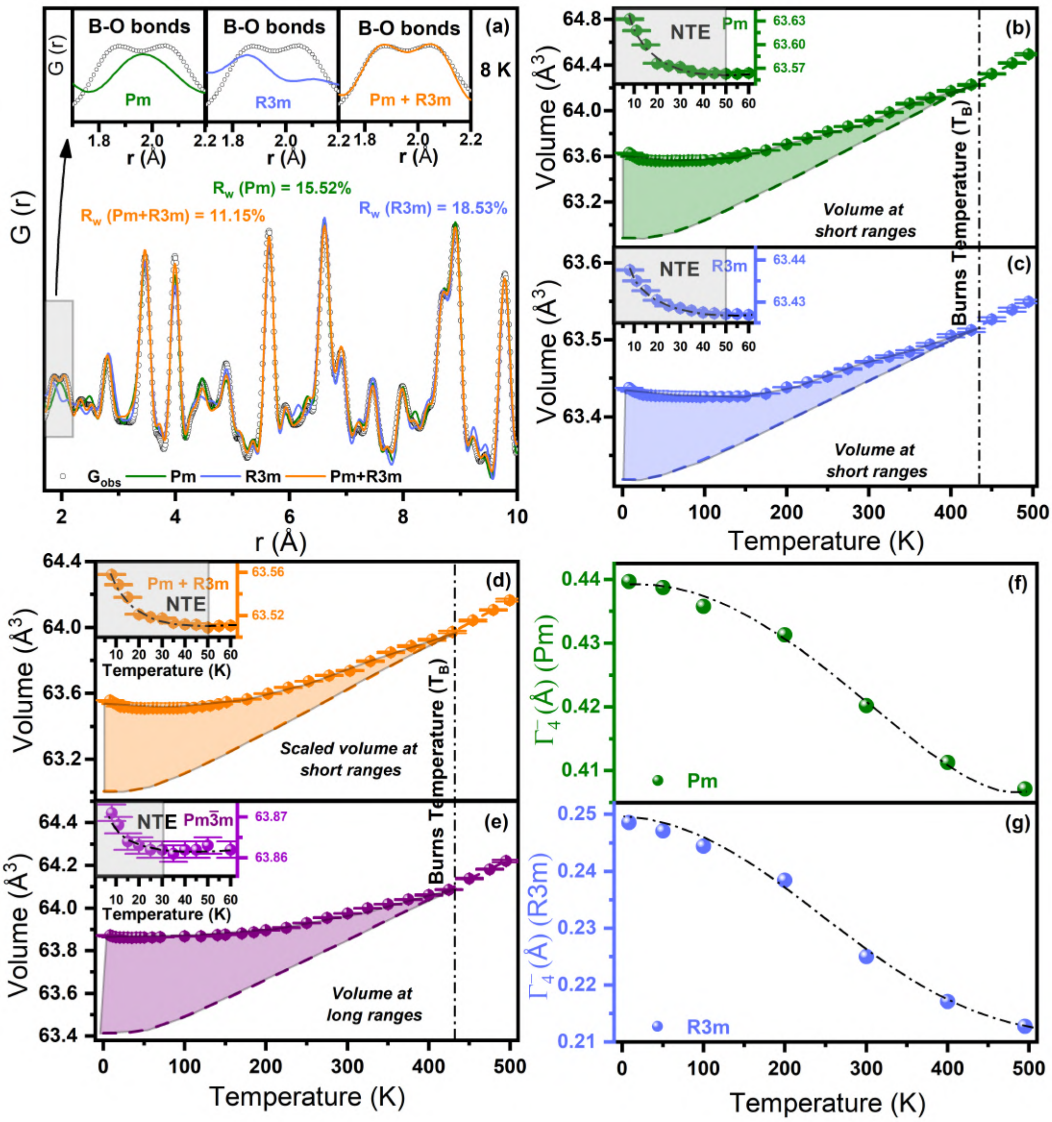

Fig. 7.6 (a) Fitting of the PDF profiles of KBST40 ceramics at 8 K using *Pm*, *R*3*m*, and *Pm*+*R*3*m* models. The inset of (a) shows the PDF profile fitting corresponding to B-O bonds. Evolution of the volume at short ranges for (b) *Pm* (green symbols), (c) *R*3*m* (blue symbols), (d) *Pm*+*R*3*m* (orange symbols), at long ranges for (e) $Pm\bar{3}m$ (purple symbols) of KBST40 for 8 K $\leq$ T $\leq$ 495 K. The insets in (b)-(e) show negative thermal expansion (NTE) observed at very low temperatures at long/short ranges. Lastly, the evolution of ferroelectric mode ($\Gamma_4^-$) as a function of temperature for (f) *Pm* and (g) *R*3*m* phase.

Å $\leq r \leq$ 10 Å. The fittings corresponding to the *Pm* and *R*3*m* models show various misfits, which are clearly visible for the first coordination sphere (*i.e.*, B-O bonds) (see insets of Fig. 7.6(a)). The best fit, along with the lowest $R_w$ value, was obtained for the two-phase model

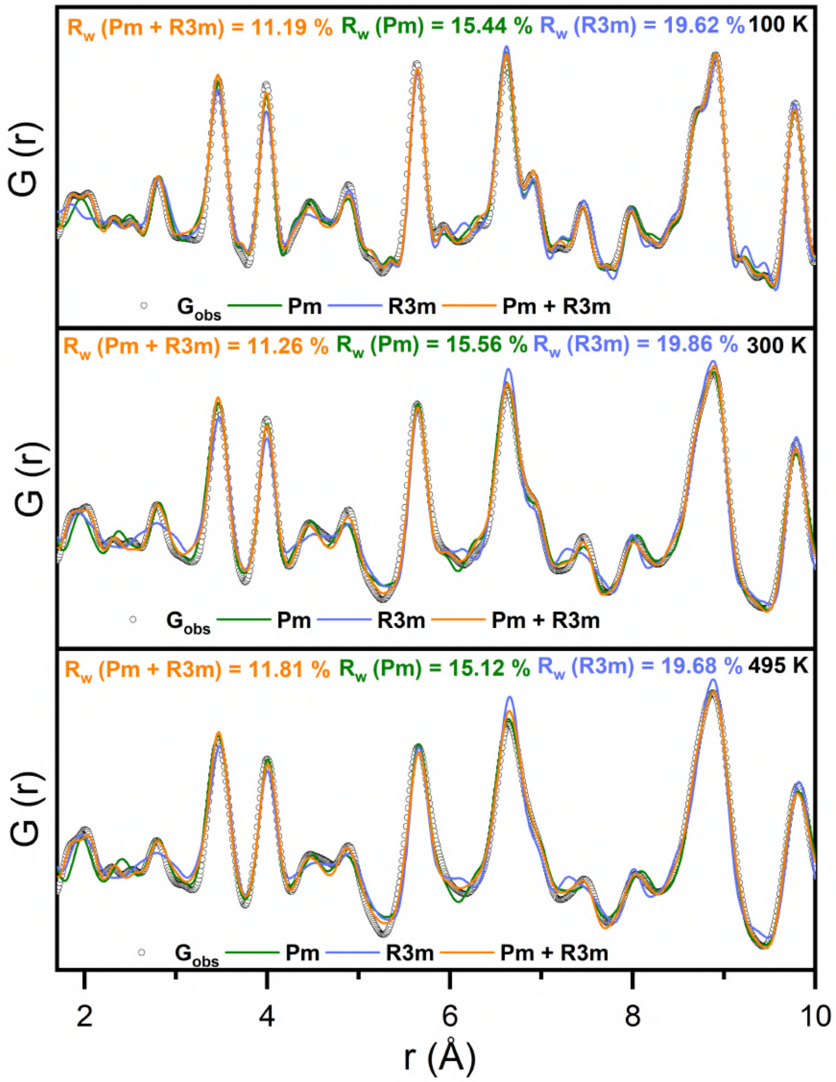

Fig. 7.7 Temperature-dependent fitting of PDF profiles using *Pm*, *R*3*m*, and (*Pm*+*R*3*m*) models for KBST40 ceramics.

(R+M) (see Fig. 7.6(a)), verifying the conclusions inferred from the temperature-dependent Raman analysis. The two phases at short ranges (1.7 Å $\leq r \leq$ 10 Å) persist up to the highest studied temperature (see Fig. 7.7). Subsequently, the refined volume for the two phases (*Pm* & *R*3*m*), as well as the cumulative weighted phase volume (summed volume weighed according to phase fractions of *Pm* and *R*3*m*), has been shown in Figs. 7.6(b)-(d). It is clearly evident from the figures that the volume becomes nearly temperature-independent

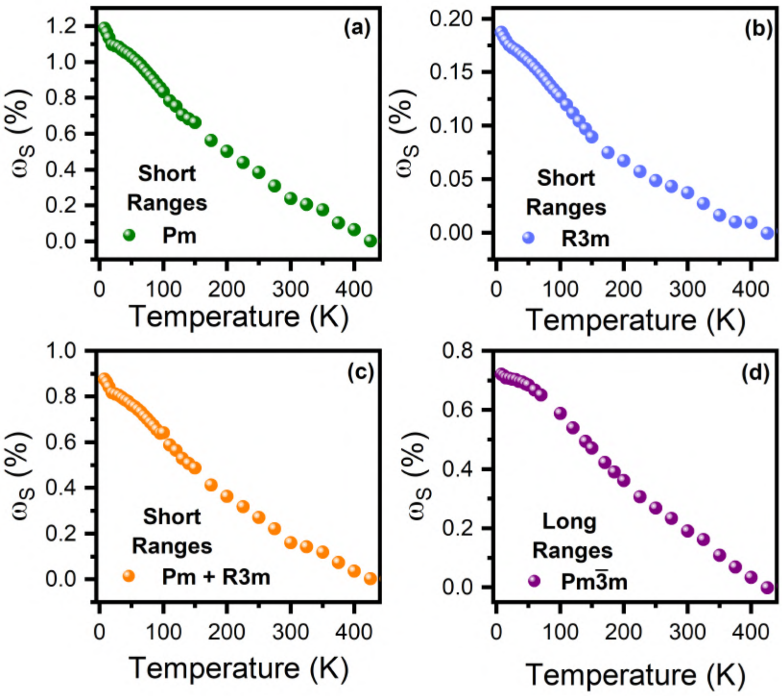

Fig. 7.8 Evolution of SVFS ($\omega_S$) as function of temperature for different phases at short/long ranges.

(*i.e.*, ZTE) at low temperatures ($T < 200$ K) and exhibits negative thermal expansion (NTE) at very low temperatures ($T < 60$ K) (see Figs. 7.6(b)-(d)). Moreover, inter-polar-cluster (nanoregions) interaction increases with decreasing temperatures [7, 118, 142], leading to enhancement in polar/ferroelectric ordering. The enhanced polar/ferroelectric ordering at low temperatures is accompanied by ferroelectrostriction, clearly evident by volume gain at low temperatures [7, 118, 142]. The ferroelectrostriction is quantified using a factor ($\omega_S$) known as spontaneous volume ferroelectrostriction (SVFS), and is defined as $\omega_S = \frac{V_{\text{exp}} - V_{\text{nm}}}{V_{\text{nm}}} \times 100$ %. Here, $V_{\text{exp}}$ is the volume at temperature $T$, and $V_{\text{nm}}$ corresponds to the nominal volume obtained after fitting $V_{\text{exp}}$ for $T \geq T_B$ (425 K $\leq T \leq$ 495 K) using Debye-Gr*ü*niesen equation [7, 19, 118]. Here, $T_B$ is known as the Burns temperature below which the nucleation and growth of polar nanoregions begin [5, 7, 22, 118]. For KBST40, $T_B$ is calculated by using temperature-dependent dielectric data (see Fig. 7.9) and can also be inferred from temperature-dependent Raman scattering data (see Fig. 7.4). SVFS for the two polar phases increases with decreasing temperatures (see Figs. 7.8(a)-(c)), suggesting an increase in ferroelectrostriction and, thereby, triggering NTE/ZTE in the material. NTE/ZTE is quantified by volumetric coefficient of thermal expansion (CTE); $\alpha_V$ = (1/V)(dV/dT) [7, 19, 118]. Very low CTE ($\alpha_V$) at low temperatures has been observed for local symmetries at short ranges (see Table 7.1). Further, the increase in polar/ferroelectric ordering at short ranges on lowering temperatures has been quantified using the frozen phonon mode approach of mode crystallography. It is well known that the condensation of a triply degenerate ferroelectric soft phonon mode *viz.*, $\Gamma_4^-$ (associated with the zone center of cubic Brillouin zone) leads to ferroelectric ordering in the dielectric material. Figures 7.6(f)-(g) depicts the evolution of $\Gamma_4^-$ phonon mode as a function of temperature for the two polar phases observed at short ranges. The amplitude of $\Gamma_4^-$ mode increases with decreasing temperature, confirming an increase in ferroelectric content/ordering in the material, consequently resulting into NTE/ZTE at short ranges [7, 118].

Table 7.1 Debye temperature ($\theta_D$), volume at 0 K ($V_0$), SVFS ($\omega_S$), and volumetric coefficient of thermal expansion (CTE; $\alpha_V$) for the phases at long/short ranges.

| Phase | $\theta_D$ | Volume at 0 K ($V_0$) | SVFS ($\omega_S$) (at 8 K) | CTE ($\alpha_V \times 10^{-6}$ K$^{-1}$) (8 K- 495 K) |
|---|---|---|---|---|
| Monoclinic<br>(Short ranges) | ≈ 220 K | 62.886 Å$^3$ | ≈ 1.19 % | −75.43 to +58.84 |
| Rhombohedral<br>(Short ranges) | ≈ 170 K | 63.319 Å$^3$ | ≈ 0.19 % | −13.66 to +8.18 |
| Monoclinic + Rhombohedral<br>(Scaled volume as per phase fraction)<br>(Short ranges) | ≈ 218 K | 63.006 Å$^3$ | ≈ 0.88 % | −49.04 to +45.98 |
| Cubic<br>(Long ranges) | ≈ 219 K | 63.414 Å$^3$ | ≈ 0.72 % | −15.66 to +30.36<br>$\alpha_l$ = −5.22 to +10.12 × 10$^{-6}$ K$^{-1}$ |

## Temperature-dependent real and imaginary parts of the dielectric constant of KBST40

Figure 7.9 depicts temperature-dependent real and imaginary parts of the dielectric constant of KBST40 ceramics at various frequencies. The inset represents the plot between the inverse of the dielectric constant ($1/\varepsilon'$) and temperature (T). Burns temperature ($T_B$) is determined using inverse dielectric plot ($1/\varepsilon'$ vs $T$) and temperature-dependent Raman scattering data (see Fig. 7.4).

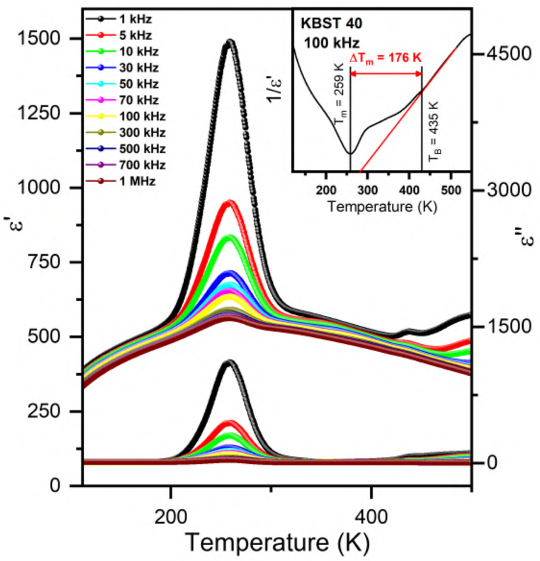

Fig. 7.9 Temperature-dependent dielectric of KBST40. The inset shows the plot between the inverse of the dielectric constant ($1/\varepsilon'$) and temperature (T). Here, $\Delta T_m$ is the difference between $T_B$ & $T_m$ and corresponds to disorder in the material [22].

Furthermore, the impact of short-range ordering on thermal expansion of KBST40 will be analyzed by analyzing temperature-dependent synchrotron X-ray diffraction (SXRD) data.

### 7.3.4 Synchrotron X-ray diffraction analysis of KBST40 ceramics

The temperature-dependent SXRD data of KBST40 ($8\ \mathrm{K} \leq T \leq 495\ \mathrm{K}$) has been analyzed to determine structural phase transition(s) as a function of temperature. The main perovskite peaks exhibit a singlet nature for $8\ \mathrm{K} \leq T \leq 495\ \mathrm{K}$, suggesting an average cubic symmetry at long ranges (see Fig. 7.10). Subsequently, the cubic structure (Space Group: $Pm\bar{3}m$) was used to refine the SXRD data [188], and the volume was plotted as a function of temperature $V(T)$. A volume gain is observed below $T_B$ (see Fig. 7.6(e)) due to ferroelectrostriction,

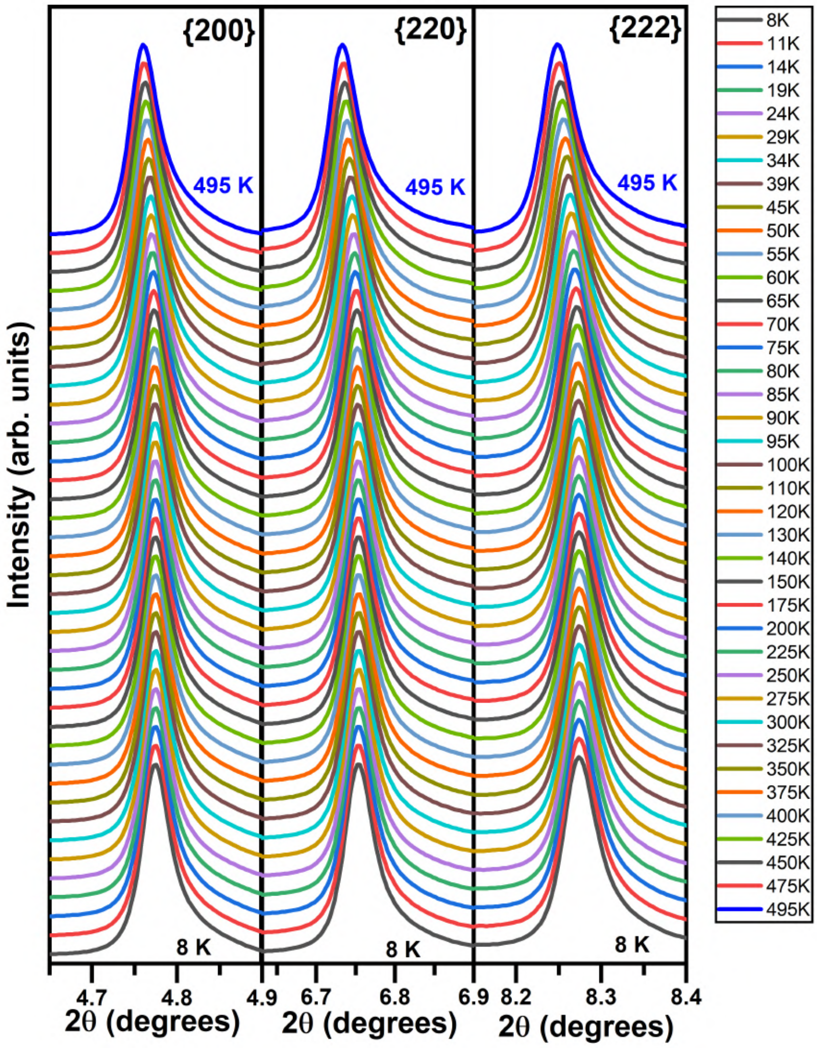

Fig. 7.10 Evolution of main perovskite peaks *viz.*, {200}, {220}, and {222} as a function of temperature for KBST40 ceramics.

which increases with decreasing temperatures (see Fig. 7.8(d)). Consequently, V($T$) at long ranges depicts ZTE at low temperatures (T < 200 K) and NTE at very low temperatures (T < 25 K) (see Fig. 7.6(e)). Moreover, for a cubic system, a linear coefficient of thermal expansion ($\alpha_l$) is calculated by using $\alpha_l = (1/3)\alpha_\text{V}$ [7, 19, 118]. For KBST40, $\alpha_l$ ranges between −5.22 to +10.12 × $10^{-6}$ $\text{K}^{-1}$ (8 K − 495 K). Further, Fig. 7.11 depicts the comparison of linear CTE ($\alpha_l$) at 100 K and 200 K for KBST20, KBST40, and KBST90 ceramics. A linear CTE value at 100 K is 0.39 × $10^{-6}$ $\text{K}^{-1}$ for KBST40, which is lower

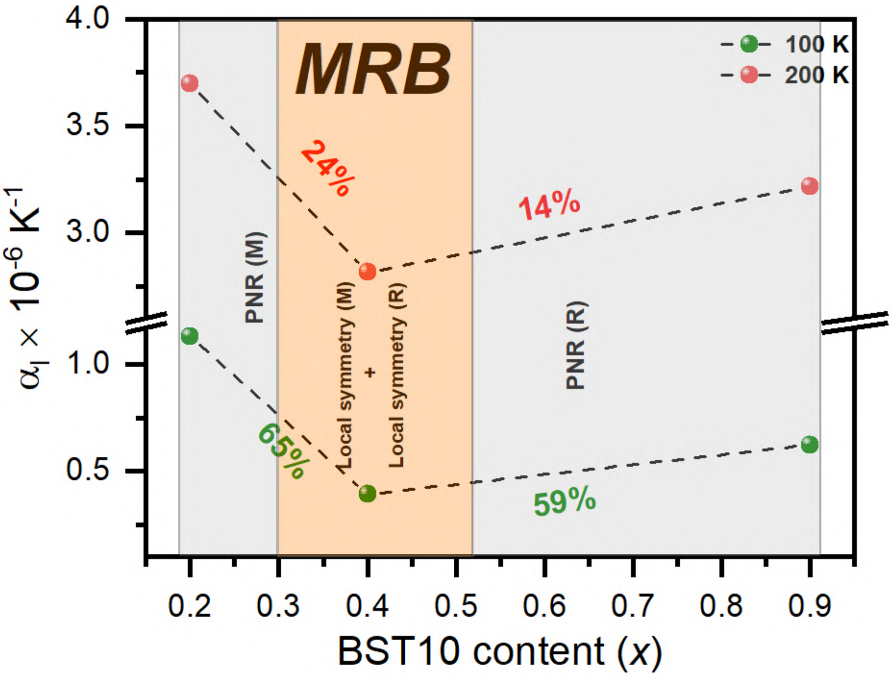

Fig. 7.11 Evolution of linear CTE ($\alpha_l$) values calculated at 100 K and 200 K for KBST20, KBST40, and KBST90 ceramics.

by 65% and 59% from its adjacent compositions *viz.*, KBST20 and KBST90. Similar lowering of CTE is observed for KBST40 at 200 K (see Fig. 7.11). Therefore, it is clearly evident from Fig. 7.11 that KBST40 demonstrates a minimum value of CTE (see Fig. 7.11) at low temperatures ($T \leq 200$ K). NTE/ZTE in KBST40 has been attributed to the cumulative effect of ordering and enhanced ferroelectric displacements (at short ranges) at low temperatures in the material with maximum disorder [22, 118]. The maximum disorder in KBST40 is due to the presence of two coexisting phases (M+R) at short ranges in an average cubic structure at long ranges, stable for a wide temperature range.

### 7.3.5 Morphotropic Relaxor Boundary in KBST$x$ ceramics

Finally, the combined analysis of X-ray diffraction, Raman scattering, and synchrotron X-ray diffraction data establishes morphotropic relaxor boundary (MRB) as a function of composition ($x$) and temperature ($T$) (see Fig. 7.12). The PNRs exhibit monoclinic symmetry for $x < 0.30$ and rhombohedral symmetry for $x > 0.50$ (represented by PNR(M) and PNR(R)) at ambient conditions in Fig. 7.12. The compositions in between (0.20 $< x < 0.60$) demonstrate the presence of two distinct symmetries *viz.*, monoclinic and rhombohedral (see Fig. 7.12) at short ranges for a wide temperature range. Moreover, an average cubic phase appears above $T_B$ ($T_B$ is determined/inferred from temperature-dependent Raman scattering data, see Fig. 7.4). Consequently, the presence of two polar phases at short ranges in an average cubic phase at long ranges with weak temperature dependence establishes MRB in KBST*x* (see Fig. 7.12).

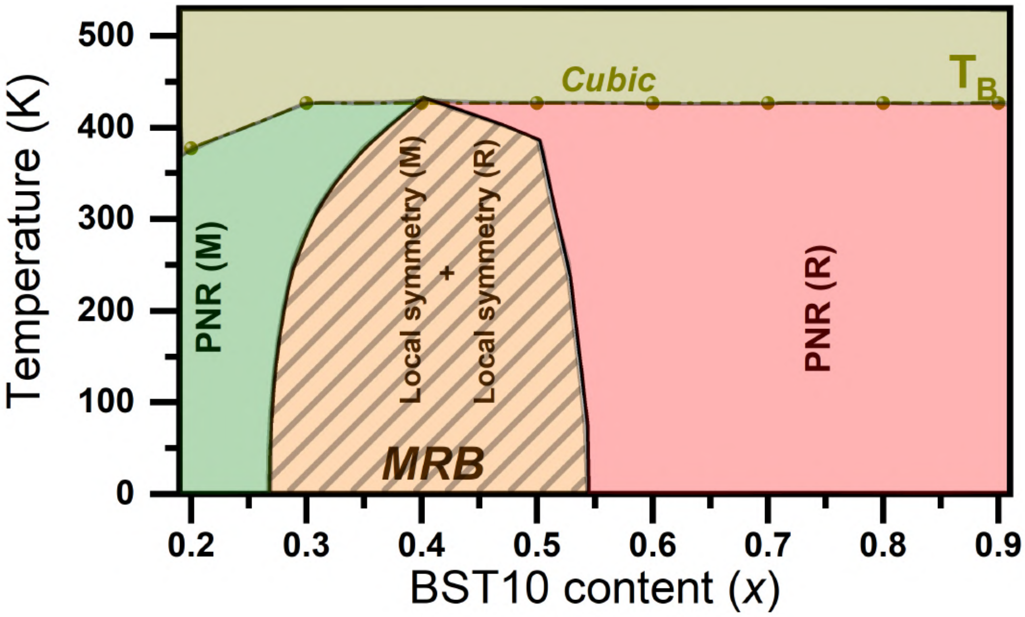

Fig. 7.12 Morphotropic Relaxor Boundary in KBST*x* ceramics.

## 7.4 Conclusion

In conclusion, a unique morphotropic relaxor boundary (MRB) has been discovered in $Ba_{0.9}Sr_{0.1}TiO_3$ (BST10) doped $K_{0.5}Na_{0.5}NbO_3$ (KNN50) *viz.*, (1-*x*)KNN50-*x*BST10 (KBST*x*), and its influence on thermal expansion has been investigated using composition-dependent X-ray diffraction, temperature-dependent Raman scattering, and synchrotron

X-ray diffraction data. The MRB composition *viz.*, KBST40 exhibits coexistence of two distinct polar symmetries *viz.*, monoclinic and rhombohedral at short ranges in an average cubic symmetry stable for a wide temperature range, in contrast to tetragonal and rhombohedral symmetries observed at short ranges in a recently discovered KNN50-based MRB [15]. Moreover, KBST40 exhibits negative/zero thermal expansion, which is clearly evident from the linear coefficient of thermal expansion (CTE) ($\alpha_l$), ranging between $-5.22$ to $+10.12 \times 10^{-6}$ K$^{-1}$ (8 K – 495 K). Further, the source of low CTE was investigated using temperature-dependent pair distribution function data. This remarkably low CTE of KBST40 at long ranges derives its origin from enhanced ferroelectric order at short ranges (demonstrated by the increase in amplitude of ferroelectric phonon mode $\Gamma_4^-$). The enhanced ferroelectric ordering results in very low CTE at short ranges, thereby transferring it to long ranges. Moreover, a comparison of thermal expansion at 100 K reveals that $\alpha_l$ of KBST40 (MRB composition with maximum vertical width $\Delta T_{R+M}$) is lower by 65% and 59% from the end compositions *viz.*, KBST20 (RFE with PNRs exhibiting monoclinic symmetry) and KBST90 (RFE with PNRs exhibiting rhombohedral symmetry). Overall, two or more relaxor ferroelectrics with distinct short-range order demonstrating low CTE can be tailored to achieve an MRB with a very low CTE, thereby opening new avenues for advancement in electronics by effective thermal management.

In the next chapter, we present a brief conclusion and future works related to the thesis.